

Engineering Surface Structure of Spinel Oxides via High-Valent Vanadium Doping for Remarkably Enhanced Electrocatalytic Oxygen Evolution Reaction

Renjie Wei,^{†,§,ⓑ} Xiuming Bu,^{†,§,ⓑ} Wei Gao,^{†,‡,§,ⓑ} Rovi Angelo B. Villaos,^{||} Genevieve Macam,^{||} Zhi-Quan Huang,^{||} Changyong Lan,^{†,§,ⓑ} Feng-Chuan Chuang,^{*,||,ⓑ} Yongquan Qu,^{‡,ⓑ} and Johnny C. Ho^{*,†,§,ⓑ}

[†]Department of Materials Science and Engineering, City University of Hong Kong, Kowloon 999077, Hong Kong

[‡]Center for Applied Chemical Research, Frontier Institute of Science and Technology, Xi'an Jiaotong University, Xi'an 710049, P. R. China

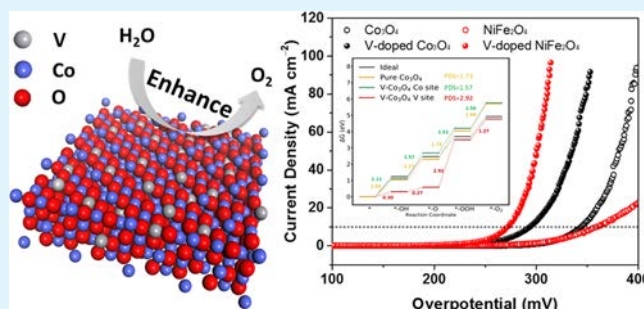
[§]Shenzhen Research Institute, City University of Hong Kong, Shenzhen 518057, P. R. China

^{||}Department of Physics, National Sun Yat-Sen University, Kaohsiung 80424, Taiwan

Supporting Information

ABSTRACT: Spinel oxides (AB_2O_4) with unique crystal structures have been widely explored as promising alternative catalysts for efficient oxygen evolution reactions; however, developing novel methods to fabricate robust, cost-effective, and high-performance spinel oxide based electrocatalysts is still a great challenge. Here, utilizing a complementary experimental and theoretical approach, pentavalent vanadium doping in the spinel oxides (i.e., Co_3O_4 and $NiFe_2O_4$) has been thoroughly investigated to engineer their surface structures for the enhanced electrocatalytic oxygen evolution reaction. Specifically, when the optimal concentration of vanadium (ca. 7.7 at. %) is incorporated into Co_3O_4 , the required overpotential to reach a certain j_{GEO} and j_{ECSA} decreases dramatically for oxygen evolution reactions in alkaline media. Even after 30 h of chronopotentiometry, the required potential for V-doped Co_3O_4 just increases by 16.3 mV, being much lower than that of the undoped one. It is observed that the pentavalent vanadium doping introduces lattice distortions and defects on the surface, which in turn exposes more active sites for reactions. DFT calculations further reveal the rate-determining step changing from the step of $*-O$ to $*-OOH$ to the step of $*-OH$ to $*-O$, while the corresponding energy barriers decrease from 1.73 to 1.57 eV accordingly after high-valent V doping. Moreover, the oxygen intermediate probing method using methanol as a probing reagent also demonstrates a stronger OH^* adsorption on the surface after V doping. When vanadium doping is performed in the inverse spinel matrix of $NiFe_2O_4$, impressive performance enhancement in the oxygen evolution reaction is as well witnessed. All these results clearly illustrate that the V doping process can not only efficiently improve the electrochemical properties of spinel transition metal oxides but also provide new insights into the design of high-performance water oxidation electrocatalysts.

KEYWORDS: spinel oxides, vanadium doping, surface engineering, electrocatalysts, oxygen evolution reaction



INTRODUCTION

The oxygen evolution reaction (OER) plays a key role in water splitting and carbon dioxide reduction processes. However, due to the intrinsic sluggish kinetics originating from a series of proton-coupled electron transfer steps, there are still substantial challenges encountered during the search of robust and cost-efficient OER electrocatalysts.^{1–3} Although noble-metal-based electrocatalysts, such as IrO_2 and RuO_2 , have been widely studied because of their inherent superior activity and stability for water oxidation under both acidic and alkaline conditions,^{4,5} their scarcity and associated high cost inevitably limit their practical applications. Therefore, exploring the

promising alternative electrocatalysts is of great interest in the community.

In general, transition-metal-based spinel oxide (AB_2O_4) is one of the most studied candidates owing to their earth abundance, low cost, unique structures, and multiple valence sites.^{6,7} Typically, the spinel oxides can be classified into three main types, namely, normal spinel, inverse spinel, and mixed spinels. It is found that their physical properties highly depend

Received: June 21, 2019

Accepted: August 15, 2019

Published: August 15, 2019

on the associated crystal structures.⁸ For example, for inverse spinels (e.g., Fe_3O_4), their short B–B bond length can facilitate the efficient electron transfer and enhance the electrical conductivity; nevertheless, normal spinels (e.g., Co_3O_4) involve longer A–B hop distances exhibiting the poor conductivity, which constitutes a major concern for electrocatalysis.⁹ Such special properties have hence attracted a lot of attention in manipulating the altering spinel structures and improving their properties for enhanced OER activities.

At the same time, engineering the surface structure of electrocatalysts has also been demonstrated as an effective route to optimize their performance.^{10–12} Based on a recent report, it is experimentally elucidated that surface Co^{2+} sites (i.e., the A site in spinel) are responsible for the formation of CoOOH , which serves as the active sites for water oxidation.¹³ This study provides a feasible strategy to enhance the OER activity of catalysts by regulating the ratio of Co^{2+} to Co^{3+} . By using the plasma-engraving strategy, Xu et al. prepared Co_3O_4 nanosheets with abundant oxygen vacancies (V_O) and showed remarkable promotion for water oxidation in which this improved OER activity can be attributed to the formation of vacancies in lowering the average valent state of Co and increasing the Co^{2+} percentage.¹⁴ Likewise, the NaBH_4 treatment is as well observed to generate surface V_O and to subsequently increase the ratio of $\text{Co}^{2+}/\text{Co}^{3+}$.^{15,16} Another common method of tuning the surface structure is to substitute the ions in the host matrix with foreign ones. For example, Zhang et al. have recently reported a facile method to introduce V_O on the CoO surface by introducing the B anion, and the vacancy-rich CoO exhibits a low overpotential of 280 mV at a current density of 10 mA cm^{-2} .¹⁷ By utilizing in situ X-ray absorption near edge structure and extended X-ray absorption fine structure spectroscopy, Liu's group experimentally pointed out that the introduced Ni^{3+} on the Ni–Co oxide surface is likely to occupy the tetrahedral sites transforming into NiOOH , which is the main active site for the OER process.¹⁸ In any case, until now, as compared with Fe, Co, Ni, and Mn, V with various valence states has been rarely studied as a dopant for electrocatalysts.^{19–21}

Enlightened by the previous works, we perform a complementary experimental and theoretical study to incorporate the high-valent vanadium cations into spinel structured Co_3O_4 nanoparticles in order to regulate their surface structures. The electrochemical results show that the pentavalent V-doped Co_3O_4 nanoparticles with ~ 7.7 at. % dopant concentration display a much better OER performance in both activity and stability than the pristine ones and other counterparts with different dopant concentrations. The integration of pentavalent V can facilitate the fast charge transfer and expose more active sites on the catalysts' surface, which results in a considerable enhancement in their activity toward OER. It is also found that the rate-determining step of the OER process changes from the step of ($^*\text{-O}$ to $^*\text{-OOH}$) to the step of ($^*\text{-OH}$ to $^*\text{-O}$) with the corresponding energy barriers decreasing from 1.73 to 1.57 eV after high-valent V doping. Similarly, V doping can as well lead to the impressive OER performance of the inverse spinel oxide of NiFe_2O_4 . All these promotions in the OER performance can be ascribed to the optimization of the catalysts' surface structures via optimal pentavalent vanadium doping.

EXPERIMENTAL SECTION

Preparation of Pristine Co_3O_4 and V-Doped Co_3O_4 Nanoparticles. In the typical preparation, 1 mmol of $\text{Co}(\text{CH}_3\text{COO})_2 \cdot 4\text{H}_2\text{O}$ was dissolved in 10 mL of absolute alcohol to obtain 0.1 M solution, while 1 mmol of oxalic acid was dissolved in 1 mL of absolute alcohol to obtain 1.0 M solution. After the complete dissolution, the oxalic acid solution was added dropwise into the $\text{Co}(\text{CH}_3\text{COO})_2$ solution. After stirring for half an hour, the mixture solution was transferred into a Teflon-lined stainless steel autoclave followed by heating at $150 \text{ }^\circ\text{C}$ for 6 h. Then it was cooled to room temperature naturally. The precipitates were collected, washed with anhydrous ethanol and deionized water, and then dried at $60 \text{ }^\circ\text{C}$ overnight. The collected precursor was subsequently calcined in air with a ramp rate of $5 \text{ }^\circ\text{C min}^{-1}$ to $400 \text{ }^\circ\text{C}$ and maintained for 2 h. For the preparation of V-doped Co_3O_4 nanoparticles with various dopant concentrations, different molar ratios of $\text{Co}(\text{CH}_3\text{COO})_2 \cdot 4\text{H}_2\text{O}$ to VCl_3 (i.e., 2:1, 3:1, 4:1, 9:1, and 19:1) were added into 10 mL of alcohol with a total concentration of 0.1 M followed by the same procedures above.

Preparation of Pristine NiFe_2O_4 and V-Doped NiFe_2O_4 . The NiFe_2O_4 sample was prepared via a sol–gel method followed by calcination according to the previous literature.²² In the typical preparation, 2.5 mmol of $\text{Ni}(\text{NO}_3)_2 \cdot 6\text{H}_2\text{O}$ and 5 mmol of $\text{Fe}(\text{NO}_3)_3 \cdot 9\text{H}_2\text{O}$ were dissolved in 25 mL of deionized water. Subsequently, 0.2 g of K30 PVP and 7.5 mmol of citric acid were added into the solution. The final solution was magnetically stirred overnight at room temperature. The obtained gel was calcinated at $400 \text{ }^\circ\text{C}$ for 2 h. After calcination, the products were washed by absolute ethanol and deionized water three times each to remove the Cl^- anion and then dried in an oven overnight. For preparing the V-doped NiFe_2O_4 , an appropriate amount of VCl_3 was added into the solution together with the Ni and Fe sources and then followed by the same procedures above.

Characterization. The crystalline structures of prepared samples were confirmed by powder X-ray diffraction (XRD, SmartLab XRD, and Bruker D2) equipped with monochromatized $\text{Cu K}\alpha$ radiation, employing a scanning rate of $0.05^\circ \text{ s}^{-1}$ in a 2θ range from 10 to 80° . The morphologies, chemical compositions, and elemental mapping were characterized by scanning electron microscopy (SEM, Philips XL30 ESEM) equipped with an energy dispersive X-ray spectrometer system and transmission electron microscopy (TEM, FEI F20). The chemical compositions of the samples were as well analyzed by inductively coupled plasma atomic emission spectrometry (ICP-AES, PerkinElmer Optima 8000). The chemical states of the surface elements were studied by using X-ray photoelectron spectroscopy (XPS, PHI 5802) using the monochromatic $\text{Al K}\alpha$ radiation under vacuum at a pressure of 1×10^{-9} torr. All the binding energies were referenced to the C 1s peak at 284.8 eV of the surface adventitious carbon. The Raman scattering spectra were obtained by a Raman spectrometer (WITec alpha300 access) with a laser of 532 nm wavelength.

Electrochemical Measurements. Typically, 5 mg of electrocatalyst samples was dispersed in a mixed solution, which includes 100 μL of DI water, 340 μL of ethanol, and 20 μL of Nafion (5 wt %) by sonication for 2 h to obtain a homogeneous ink. Then 10 μL of ink was drop-casted on the polished glassy carbon (GC) electrode with a diameter of 5 mm, resulting in a mass loading of about 0.553 mg cm^{-2} . The fabricated electrodes were dried at room temperature naturally. Except for the estimation of double-layer capacitance (C_{dl}), all the electrochemical tests were investigated on a Gamry 300 electrochemical workstation equipped with a standard three-electrode configuration under $25 \text{ }^\circ\text{C}$ using a constant temperature bath. The fabricated GC, saturated calomel electrode (SCE), and carbon rod were used as the working electrode, reference electrode, and counter electrode, respectively. 1 M KOH solution was used as the electrolyte. The reported potentials in this work were calibrated to the reversible hydrogen electrode (RHE) using eq 1:

$$E_{\text{RHE}} = E_{\text{SCE}} + 0.2415 + 0.059\text{pH} \quad (1)$$

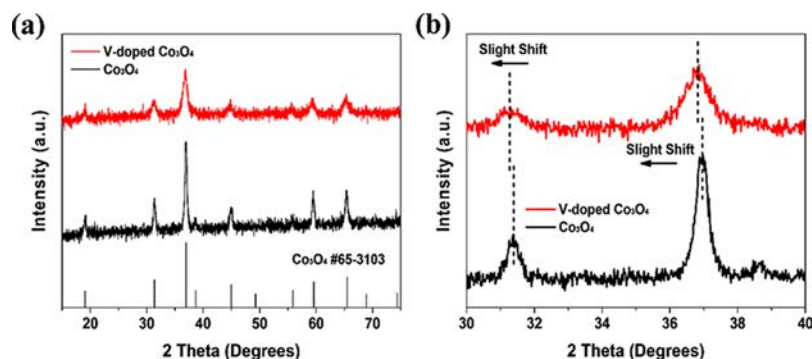
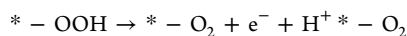
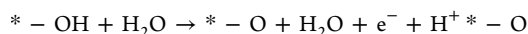
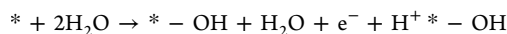


Figure 1. Typical XRD patterns of (a) pristine Co_3O_4 and V-doped Co_3O_4 and (b) corresponding magnified XRD patterns.

For activating the electrocatalysts, 20 cycles of cyclic voltammetry were conducted first within a potential window from 0.1 to 0.7 V versus SCE at a scan rate of 100 mV s^{-1} without any iR -drop compensation. Linear sweep voltammetry (LSV) with a scan rate of 1 mV s^{-1} was conducted to estimate the OER performance within a potential window from 0.15 to 0.65 V versus SCE. Electrochemical impedance spectroscopy (EIS) was applied in the frequency range between 0.05 Hz and 300 kHz at an ac voltage of 10 mV rms to evaluate the charge transfer resistance. The electrochemically active surface area (ECSA) was estimated from the electrochemical double-layer capacitance (C_{dl}) of the catalytic surface.^{23–25} For estimating the C_{dl} , CHI 660E was used to record the CV curves under different scan rates (2, 4, 6, 8, 10 mV s^{-1}).

DFT Calculations. First-principles calculation was performed in the spin-polarized density functional theory framework as implemented in the Vienna ab initio simulation package (VASP).^{26–29} Generalized gradient approximation in the Perdew–Burke–Ernzerhof (PBE) functional was applied to describe the electron exchange–correlation interaction with the projector augmented wave (PAW) potentials.^{30,31} The energy cutoff was set at 400 eV. The structure was optimized until the forces were less than 0.01 eV \AA^{-1} and self-consistent calculations were converged until 10^{-5} eV. The Brillouin zone of a six-layer Co_3O_4 (100) slab was sampled using $10 \times 10 \times 1$ Monkhorst–Pack grids with a vacuum of $\sim 10 \text{ \AA}$.³²

The reaction steps are as follows³³ where * means substrate:



The adsorption energies of intermediates (O, OH, OOH, and O_2) on the substrate were calculated using eqs 2–5:³⁴

$$\Delta E_{*-\text{OH}} = E_{\text{Sub}+\text{OH}} - E_{\text{Sub}} - \left(E_{\text{H}_2\text{O}} - \frac{1}{2} E_{\text{H}_2} \right) \quad (2)$$

$$\Delta E_{*-\text{O}} = E_{\text{Sub}+\text{O}} - E_{\text{Sub}} - (E_{\text{H}_2\text{O}} - E_{\text{H}_2}) \quad (3)$$

$$\Delta E_{*-\text{OOH}} = E_{\text{Sub}+\text{OOH}} - E_{\text{Sub}} - \left(2E_{\text{H}_2\text{O}} - \frac{3}{2} E_{\text{H}_2} \right) \quad (4)$$

$$\Delta E_{*-\text{O}_2} = E_{\text{Sub}+\text{O}_2} - E_{\text{Sub}} - (2E_{\text{H}_2\text{O}} - 2E_{\text{H}_2}) \quad (5)$$

where $\Delta E_{*-\text{OH}}$, $\Delta E_{*-\text{O}}$, $\Delta E_{*-\text{OOH}}$, and $\Delta E_{*-\text{O}_2}$ are adsorption energies (eV); $E_{\text{Sub}+\text{OH}}$, $E_{\text{Sub}+\text{O}}$, $E_{\text{Sub}+\text{OOH}}$, and $E_{\text{Sub}+\text{O}_2}$ are total energies (eV) of the substrate with adsorbed intermediates; E_{Sub} is the total energy (eV) of the clean substrate; $E_{\text{H}_2\text{O}}$ is the total energy (eV) of an isolated H_2O molecule; and E_{H_2} is the total energy (eV) of an isolated H_2 molecule.

The Gibbs free energy change (ΔG) of the chemical reaction, as compared to the free Gibbs energy of the clean surface, was calculated using eq 6:

$$\Delta G = \Delta E + \Delta \text{ZPE} - T \Delta S \quad (6)$$

where ΔE , ΔZPE , T , and S denote the calculated adsorption energy of intermediates, zero point energy, temperature, and entropy, respectively. We note that ΔZPE is negligible and the pH level was not considered in our calculations. Thus, for each reaction coordinate, ΔG was then calculated using eqs 7–10:

$$\Delta G_{*-\text{OH}} = \Delta E_{*-\text{OH}} - T \left[- \left(S_{\text{H}_2\text{O}} - \frac{1}{2} S_{\text{H}_2} \right) \right] \quad (7)$$

$$\Delta G_{*-\text{O}} = E_{*-\text{O}} - T [- (S_{\text{H}_2\text{O}} - S_{\text{H}_2})] \quad (8)$$

$$\Delta G_{*-\text{OOH}} = \Delta E_{*-\text{OOH}} - T \left[- \left(2S_{\text{H}_2\text{O}} - \frac{3}{2} S_{\text{H}_2} \right) \right] \quad (9)$$

$$\Delta G_{*-\text{O}_2} = \Delta E_{*-\text{O}_2} - T [- (2S_{\text{H}_2\text{O}} - 2S_{\text{H}_2})] \quad (10)$$

where at $T = 300 \text{ K}$, $TS_{\text{H}_2} = 0.41$, and $TS_{\text{H}_2\text{O}} = 0.67$.³⁴

The reversible potentials, with respect to the ideal catalyst, are given by eqs 11–14:

$$\Delta G_0 = \Delta G_{*-\text{OH}} - \Delta G_{*-\text{O}} - \Delta U_{\text{ideal}} \quad (11)$$

$$\Delta G_1 = \Delta G_{*-\text{O}} - \Delta G_{*-\text{OH}} - \Delta U_{\text{ideal}} \quad (12)$$

$$\Delta G_2 = \Delta G_{*-\text{OOH}} - \Delta G_{*-\text{O}} - \Delta U_{\text{ideal}} \quad (13)$$

$$\Delta G_3 = \Delta G_{*-\text{O}_2} - \Delta G_{*-\text{OOH}} - \Delta U_{\text{ideal}} \quad (14)$$

where $\Delta U_{\text{ideal}} = 1.23 \text{ eV}$.³⁴

RESULTS AND DISCUSSION

At first, the crystal phases of V-doped and undoped samples are evaluated by XRD. As shown in Figure 1a, both XRD patterns can be identified as the cubic Co_3O_4 phase. No characteristic peaks for other phases are observed. In comparison with that of Co_3O_4 , all the peaks of V-doped Co_3O_4 become broader and get decreased in the intensity, suggesting that the V doping leads to the reduction of both crystallite size and crystallinity. Besides, there is a slight shift toward a lower 2θ value after vanadium doping as given in Figure 1b, which demonstrates the successful incorporation of V into the host matrix. Similar changes have also been found in other samples with different initial precursor ratios as displayed in Figure S1. To be specific, we prepare various samples with five different starting precursor ratios of Co to V (i.e., 2:1, 3:1, 4:1, 9:1, and 19:1). Even at a high ratio of 2:1, there is not any additional diffraction peaks observed, suggesting that no trace of separated phase or no other phases such as vanadium

(hydro-)oxides are formed here. In the following discussion, we would concentrate on the study with an optimal initial precursor ratio of 4:1 as an example.

Apart from that, the morphologies and elemental compositions of prepared samples are also characterized. Comparing with the SEM images of pristine Co_3O_4 (Figure S2a,c), there is not any significant change found on the morphology of V-doped Co_3O_4 (Figure S2b,d). Elemental mapping shows that Co, V, and O are distributed homogeneously (Figure S2e). Both samples are composed of multiple nanorods and small irregular nanoparticles. The average ratio of Co to V is found to be about 12:1 (Figure S2f), which means that a dopant concentration of ~ 7.7 at. % is obtained. Notably, the dopant concentration can be regulated via introducing different initial precursor molar ratios of Co to V as demonstrated by the EDS and ICP-AES analysis (Tables S1 and S2).

Simultaneously, TEM and HRTEM can provide more details about the morphologies and surface structures of the samples. As illustrated in Figure 2a,d, both the pristine Co_3O_4

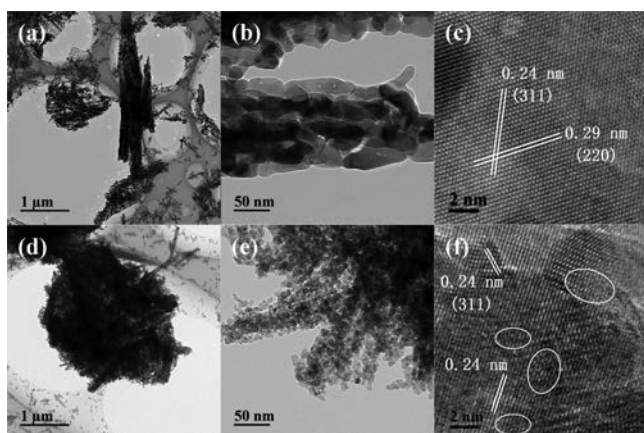


Figure 2. Typical TEM and HRTEM images of (a–c) pristine Co_3O_4 and (d–f) V-doped Co_3O_4 .

and V-doped Co_3O_4 exhibit the aggregation of small nanoparticles and nanoplates, which are consistent with the SEM results above. However, the magnified images in Figure 2b,e show that the average diameter of V-doped Co_3O_4 nanoparticles is much smaller than that of the pristine one. Moreover, the clear lattice fringes of an individual pristine Co_3O_4 nanoplate are observed with lattice spacings of 0.24 and 0.29 nm, which are assigned to the (311) and (220) planes of

cubic Co_3O_4 , respectively (Figure 2c). In contrast, the HRTEM image in Figure 2f suggests that the V-doped Co_3O_4 nanoparticle features the lower crystallinity and the smaller grain size than pristine Co_3O_4 , which are consistent with the XRD results above. Meanwhile, both regular and twisted atomic arrangements (marked by white ovals), as well as the lattice defects, are witnessed on the surface of the V-doped Co_3O_4 nanoplate. The existence of surface defects may change the vibrational modes in the system.³⁵ Figure S3 shows the Raman spectrum of pristine Co_3O_4 and V-doped Co_3O_4 , and there is an obvious blue shift after V doping. This kind of surface lattice distortion probably originates from the localized Coulomb interaction around the V atoms arising from the introduction of the incoordinate electron spin.³⁶ Such distortions and defects imply the presence of more dangling bonds and surface unsaturation, which are anticipated to increase the electronic conductivity and the number of active sites of the catalysts, as well as to decrease their surface energy, being advantageous to electrocatalysis.^{37–39}

In addition, X-ray photoelectron spectroscopy (XPS) is performed to assess the surface chemical compositions and the chemical states of fabricated electrocatalysts. All the XPS spectra are calibrated by using the adventitious carbon peak at 284.8 eV (Figure S4a). As depicted in Figure 3a, there are two characteristic peaks observed at 517.0 and 524.4 eV with a spin-energy separation of ~ 7.4 eV, which can be assigned to V $2p_{3/2}$ and V $2p_{1/2}$, respectively, demonstrating the existence of vanadium on the surface in the form of V^{5+} .⁴⁰ Figure 3b demonstrates the high-resolution XPS profiles of Co 2p for both V-doped and undoped Co_3O_4 . Two main peaks witnessed at 779.7 and 794.8 eV with two weak satellite peaks can be attributed to Co $2p_{1/2}$ and $2p_{3/2}$ spin–orbit split components, respectively.⁴¹ After V doping, both Co 2p core level peaks shift to higher binding energies of about 780.3 and 795.4 eV. These increases of the binding energy can be a clear evidence of the successful substitution of V(V) for Co in which the electronegativity of V^{5+} (2.03) is larger than those of Co^{2+} (1.38 LS, 1.32 HS) and Co^{3+} (1.69 LS, 1.62 HS);^{42,43} therefore, the peak shift of Co 2p spectra toward the higher energy is for the V-doped catalyst. Also, a similar shift is observed for O 1s XPS profiles here (Figure S4b). Meanwhile, the two fitted peaks allocated at 779.5 and 780.6 eV for Co $2p_{3/2}$ can be assigned to Co^{3+} and Co^{2+} , respectively. In general, once the high-valent ions are doped into the host matrix with relative low-valent states, the electronic structure of the host will be modified accordingly. In this case, as

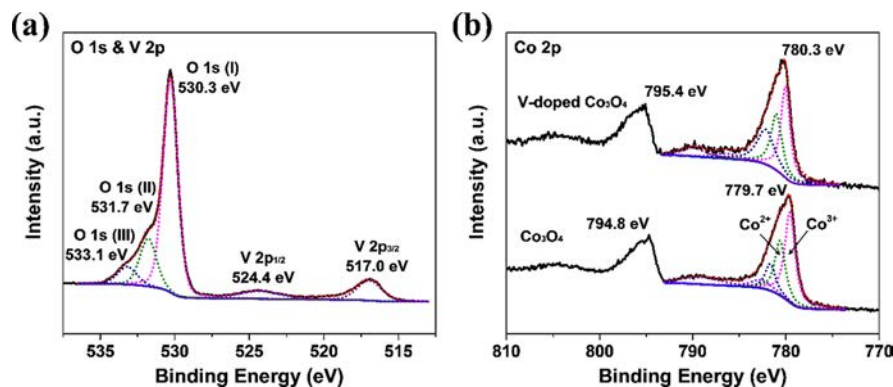


Figure 3. XPS profiles of (a) O 1s and V 2p of V-doped Co_3O_4 , (b) Co 2p of pristine Co_3O_4 and V-doped Co_3O_4 .

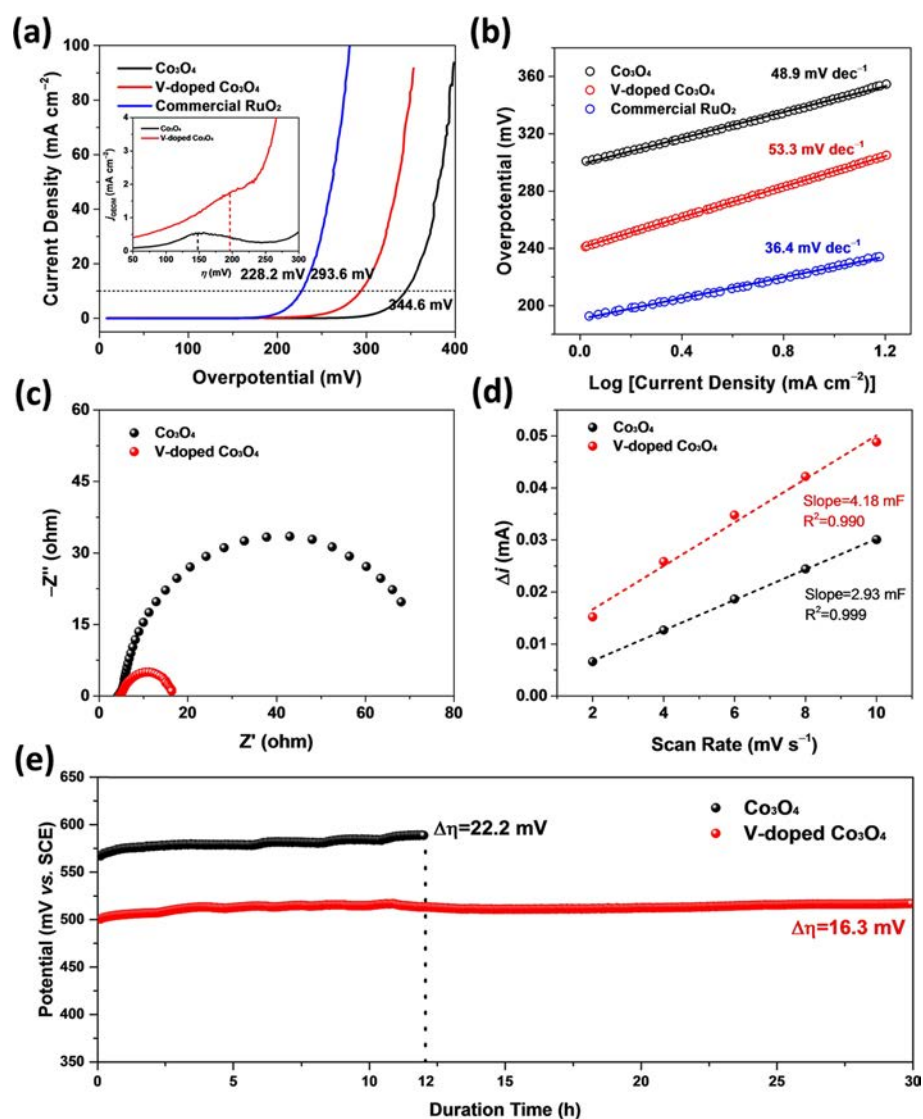


Figure 4. Electrocatalytic performance. (a) LSV curves of Co₃O₄, V-doped Co₃O₄, and commercial RuO₂ with a scan rate of 1 mV s⁻¹. The inset shows the partially enlarged LSV curves around the redox peaks of Co₃O₄ and V-doped Co₃O₄. (b) Corresponding Tafel plots. (c) Nyquist plots with frequency from 300000 to 0.05 Hz at a dc voltage of 0.5 V vs SCE. (d) Double-layer capacitance (C_{dl}) estimation using voltammetry method between 0.15 and 0.2 V vs SCE at various scan rates (2, 4, 6, 8, 10 mV s⁻¹) and (e) chronopotentiometric stability at a current density of 5 mA cm⁻².

compared with the pristine Co₃O₄, the ratio of Co²⁺/Co³⁺ for V-doped Co₃O₄ increased from 0.62 to 0.74, indicating the changes of the electronic structure of the V-doped catalyst.

To shed light on the electrochemical performance, the V-doped Co₃O₄ catalyst is thoroughly investigated for electrochemical water oxidation in O₂-saturated 1.0 M KOH solution. For comparison, pristine Co₃O₄ and others with different doping concentrations are also characterized under the same conditions. As shown in Figure 4a, the overpotential for reaching a current density (j_{GEOM}) of 10 mA cm⁻² is found to decrease significantly from 344.6 to 293.6 mV after V doping. For a direct comparison, a state of the art OER electrocatalyst, commercial RuO₂, was chosen as the comparison counterpart. It requires 228.2 mV to reach the fixed current density. At an overpotential of 350 mV, the V(V)-doped Co₃O₄ catalyst can deliver a current density of 84 mA cm⁻², which is about 7-fold higher than that of the pristine Co₃O₄. The peak located at an overpotential of ~150 mV (1.38 V vs RHE) for the pristine Co₃O₄ is due to the oxidation of Co³⁺ to Co⁴⁺.⁴⁴ Because of

the higher electronegativity of V(V), its incorporation into the host lattice of Co₃O₄ will further lower the valence state of Co, resulting in an obvious anodic shift of the oxidation peak as depicted in the figure inset of the enlarged LSV curves.⁴⁵ On the other hand, the Tafel slopes of pristine Co₃O₄ and V-doped Co₃O₄ are evaluated to be 48.9 and 53.3 mV dec⁻¹, respectively (Figure 4b). In order to illuminate the remarkable enhancement in OER performance, charge transfer resistance (R_{ct}) and double-layer capacitance (C_{dl}) are carefully assessed by EIS and voltammetry methods. Figure 4c displays that the V-doped Co₃O₄ sample has a much smaller semicircle radius than pristine Co₃O₄, indicating a much lower charge transfer resistance of V-doped Co₃O₄ during the OER process. Moreover, a C_{dl} value of 2.09 mF is obtained for the V-doped Co₃O₄ sample being much higher than that of the pristine Co₃O₄ ($C_{dl} = 1.46$ mF) (Figure 4d), suggesting that the former one possesses a larger electrochemically active surface area (ECSA). Notably, the ECSA normalized LSV curves and corresponding Tafel slopes are also evaluated as

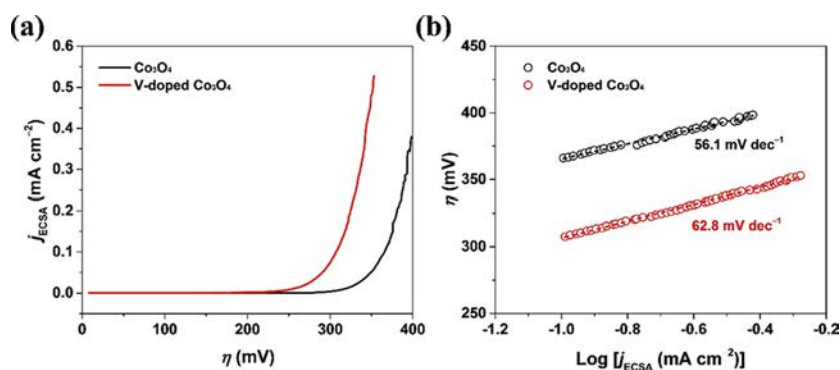


Figure 5. ECSA normalized (a) LSV curves and corresponding (b) Tafel slopes for pristine Co_3O_4 and V-doped Co_3O_4 nanoparticles. The reported specific capacitance (C_{dl}) for Co is about $43 \mu\text{F cm}^{-2}$. From the C_{dl} estimation, the capacitances for pristine and V-doped Co_3O_4 are 2.09 and 1.46 mF. $\text{ECSA} = \frac{C_{dl}}{C_{dl,ref}}$.

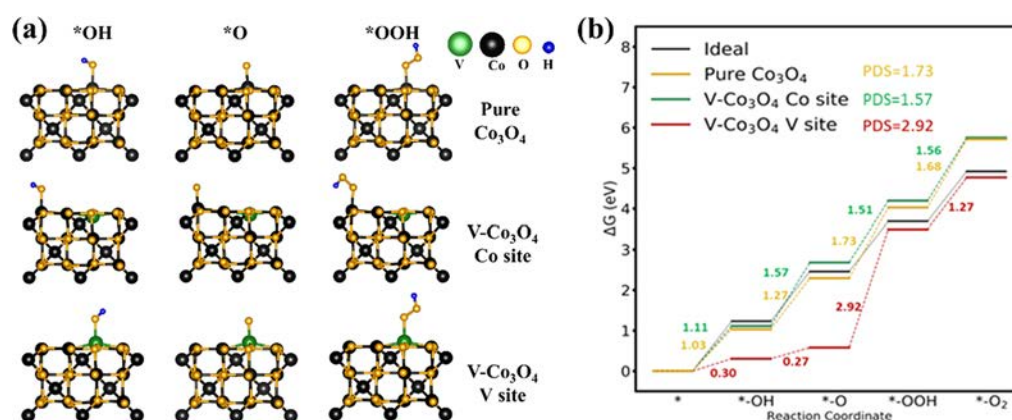


Figure 6. (a) Atomic structure of optimized six-layer Co_3O_4 . (b) Gibbs free energy landscape.

displayed in Figure 5 where the same consistent results are obtained. The specific capacitance (C_{dl}) for Co here is $43 \mu\text{F cm}^{-2}$ as referred to the previous report.²⁴

In view of the critical importance of V doping for the above electrochemical performance enhancement, other samples with various dopant concentrations are also investigated. As shown in Figure S5a,b, all the samples with vanadium doping display the superior water oxidation performance as compared with the undoped Co_3O_4 , demonstrating that V doping is beneficial for boosting the OER kinetics. Such improvement can be attributed to the optimization of the local coordination environment and surface electronic structure after the high-valent vanadium incorporation into the host matrix.²⁰ Among them, the sample with 7.7 at. % dopant concentration outperforms other samples, following the order $9:1 > 3:1 > 2:1 > 19:1$ (initial ratio of Co:V), indicating that the OER activity is highly dependent on the dopant concentration. EIS and C_{dl} estimations are as well carried out to look into the OER performance trend as described in Figures S5c,d and S6. At the higher dopant concentration, the enhancement in OER activity is mainly ascribed to the decrease of charge transfer resistance of the catalyst. However, at the lower dopant concentration, the performance improvement results from a combination of factors, including the decrease of charge transfer resistance and the increase of the number of active sites of the catalyst.

Furthermore, catalytic stability is another important parameter to evaluate the catalytic performance especially for

practical applications; hence, chronopotentiometry at a current density of 5 mA cm^{-2} is utilized to assess the electrochemical stability of different catalysts here. It should be noted that a constant current density of 10 mA cm^{-2} is typically used for this process; however, after a long duration of the test, the inked sample deposited on the GC electrode is prone to peeling off at such current density as shown in Figure S7. In any case, Figure 4e illustrates that the required overpotential for V-doped Co_3O_4 is only increased to about 16.3 mV after 30 h. In contrast, for pristine Co_3O_4 , the overpotential increases to around 22.2 mV after only 12 h, indicating that the incorporation of vanadium can as well effectively promote the catalytic stability of Co_3O_4 . TEM and HRTEM images of the sample after the stability test are shown in Figure S8. There is not any obvious change in the morphology, size, and crystal structure after the chronopotentiometry test except for the formation of an amorphous layer near the surface. Also, Figure S9 shows the comparison of XPS profiles of V-doped catalysts before and after the OER process. It is clear that there is no obvious peak shift or change of Co 2p profiles after OER. As to the V 2p profiles, the peak intensity decreases significantly after the OER process where this can be attributed to the corrosion of doped vanadium. All these results indicate the good stability of V-doped Co_3O_4 catalysts for OER.

In order to further understand the experimental results as well as the corresponding OER performance enhancement mechanism of V-doped Co_3O_4 catalysts, the detailed DFT simulation is performed. Specifically, the OER steps for both pristine and V-doped Co_3O_4 surfaces are simulated by

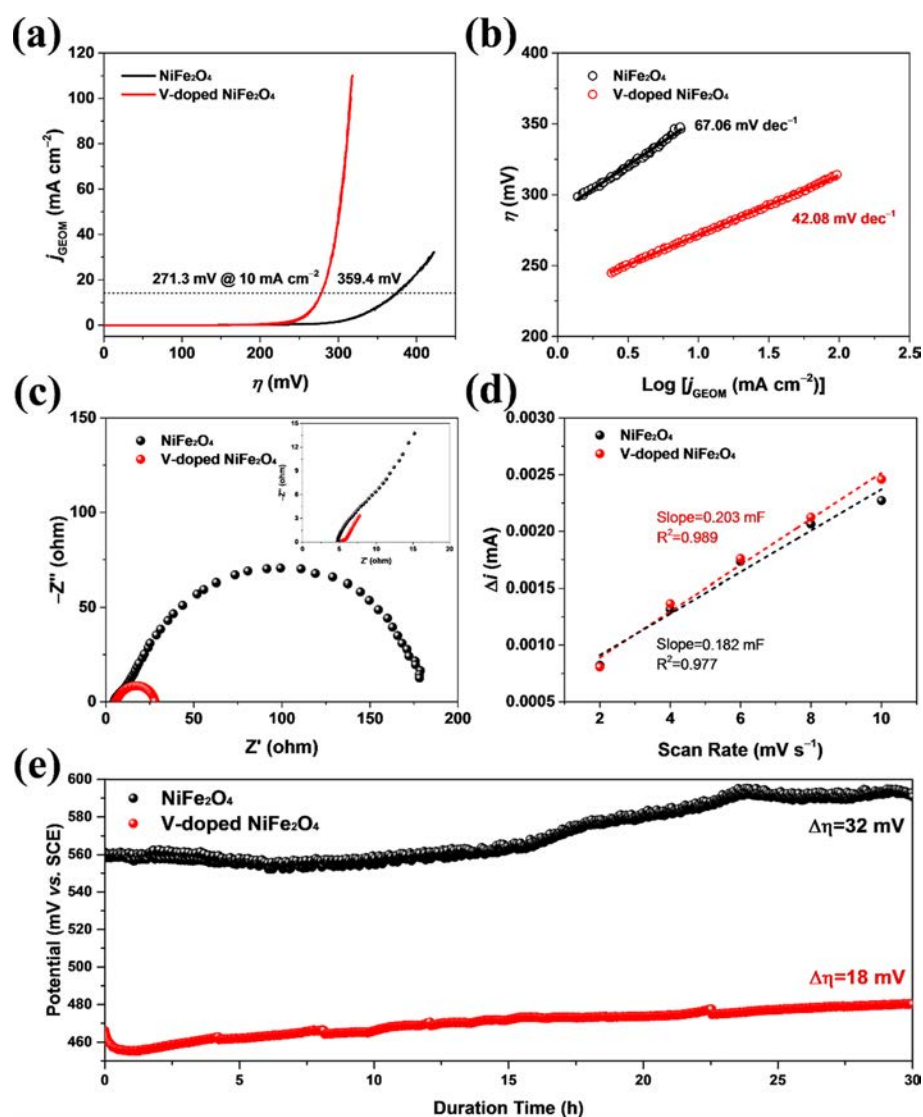


Figure 7. Electrocatalytic performances of NiFe_2O_4 and V-doped NiFe_2O_4 . (a) LSV curves, (b) Tafel plots, (c) Nyquist plots with the frequency from 300000 Hz to 0.05 Hz at a dc voltage of 0.45 V vs SCE; the inset is the Nyquist plots at high frequency (d) double-layer capacitance (C_{dl}) estimation using voltammetry method between 0 and 0.1 V vs SCE at various scan rates (2, 4, 6, 8, 10 mV s^{-1}) and (e) chronopotentiometric stability at a current density of 5 mA cm^{-2} for 30 h.

constructing the Co_3O_4 (100) surface with six layers from the optimized bulk structure. The V atom is substitutionally doped into the topmost first layer of Co_3O_4 , while the corresponding surface structures with different intermediates are shown in Figure 6a. After obtaining the optimized structures, we then compared and analyzed the Gibbs free energy profile of the associated OER process to gain insights on the electrocatalytic performances of pure and V-doped Co_3O_4 (Figure 6b). For an alkaline medium, the OER process consists of five reaction steps involving electron transfer accompanied by proton expulsion.⁴⁶ Different adsorption sites for $[\text{OH}^-]$ are first systematically investigated for both pure and V-doped catalyst surfaces. It is found that the adsorption sites preferred by $[\text{OH}^-]$ are on top of the Co atom for undoped Co_3O_4 , whereas the preferred site changes from on top of the Co atom to on top of the V atom for the V-doped Co_3O_4 surface. Throughout the processes, the V site has the lowest energy configuration as compared with the Co site of either V-doped or clean Co_3O_4 . However, if the V atom acts as the active site (red line), it has the largest energy difference of 2.92 eV in the

step of $^*\text{-O}$ to $^*\text{-OOH}$, being similar to the one reported in the previous literature.²¹ On the other hand, as given in Figure 6b, the orange line (i.e., the Co site on the clean Co_3O_4 surface) shows that the rate-determining step is located between the $^*\text{-O}$ and $^*\text{-OOH}$ intermediates with a ΔG of 1.73 eV, which is in perfect agreement with previous studies on the pure Co_3O_4 (001) surface.^{47,48} After V doping, the rate-determining step is changed and located between $^*\text{-OH}$ and $^*\text{-O}$. Moreover, the calculated Gibbs free energy change is 1.57 eV, which is the smallest among all the calculation values, demonstrating that the top Co site of V-doped Co_3O_4 contributes to the best catalytic site among the three configurations. As a result, the barrier of OER is subsequently reduced from 1.73 eV on clean Co_3O_4 to 1.57 eV on V-doped Co_3O_4 , suggesting the performance enhancement due to V doping here. To have a better understanding about the kinetic change in the OER process after V doping, we adopt a general experimental approach to probe the adsorption intermediates, which has been proposed by Liu's group⁴⁹ recently. In this method, methanol is employed as a probing reagent, which can easily

capture the oxygen intermediates (especially for *OH). As shown in Figure S10, in comparison with the methanol oxidation reaction (MOR) current on pure Co_3O_4 (black line), a much higher MOR current can be observed for V-doped Co_3O_4 (red line), demonstrating that, during the OER process, the concentration of OH^* on the surface of V-doped Co_3O_4 is much higher than that of Co_3O_4 . This observation might be the result of the rate-determining step changing from step three (M-O to M-OOH) to step two (M-OH to M-O).

Inspired by the impressive effect of V doping for Co_3O_4 , we further incorporated V into the inverse spinel metal oxide of NiFe_2O_4 . Similar to the case of spinel structured Co_3O_4 , all the XRD peaks become broader and the crystallinity of NiFe_2O_4 is decreased after the introduction of V into the host lattice (Figure S11). The incorporation of V would also lead to the formation of more Fe_2O_3 phase within the crystal. Typical SEM and TEM images display the obvious porous structures for both undoped and V-doped samples where this porosity probably comes from the calcination of the dry gel (Figures S12 and S13). The elemental mapping shows that Ni, Fe, and V are distributed homogeneously (Figure S14). Moreover, the V-doped sample features the lower crystallinity, which agrees with the XRD results above, even though there are some amorphous parts observed near the fringe, which has been demonstrated with the better OER activities as compared with their crystalline counterparts.^{50–52} Interestingly, as shown in Figure 7a, in order to reach a current density of 10 mA cm^{-2} , the V-doped NiFe_2O_4 catalyst only requires an overpotential of $\sim 271.3 \text{ mV}$, which is ~ 90 and 20 mV lower than the undoped NiFe_2O_4 and V-doped Co_3O_4 , respectively. Apparent decreases in both Tafel slope and semicircular diameter of the Nyquist plot are also witnessed, which implies the favorable kinetic behavior toward electrochemical OER and the faster charge transfer on the V-doped sample (Figure 7b,c). Nevertheless, the ECSA of NiFe_2O_4 does not change much after V doping (Figure 7d). The durability of the V-doped catalyst is also improved (Figure 7e). Specifically, the required overpotential of V-doped NiFe_2O_4 increases by $\sim 18 \text{ mV}$ as compared with the undoped one of 32 mV after 30 h of chronopotentiometry. It should be noticed that, after being normalized with ECSA, there is an obvious change in the Tafel slope, decreasing from 129.4 to 43.9 mV dec^{-1} after incorporating V into the host catalyst (Figure S15). All these results evidently illustrate the OER performance enhancement associated with V doping into the inverse spinel oxide of NiFe_2O_4 .

CONCLUSIONS

In summary, we prepare a series of V(V)-doped Co_3O_4 nanoparticles with various dopant concentrations and demonstrate that the incorporation of V(V) into the host catalyst can dramatically enhance its electrocatalytic activity and stability of the OER process. The introduction of high-valent V dopants is found to make the surface lattice more disordered, creating more surface defects and subsequently optimizing surface electronic structures of the host. In this case, the resulting efficient charge transfer ability and the more active sites exposed on the surface would yield the lower overpotential and the higher stability of the catalyst for water oxidation. Importantly, our DFT calculation results agree well with the experimental observation where a decrease in the barrier of the rate-determining step is demonstrated. In addition, a methanol oxidation probing method has been applied to illustrate the RDS change in this work. Despite this, V doping is also proven

to be an efficacious way to improve the electrocatalytic performance of another inverse spinel metal oxide of NiFe_2O_4 . All these findings can provide further insights into the rational design of high-performance electrocatalysts for water oxidation.

ASSOCIATED CONTENT

Supporting Information

The Supporting Information is available free of charge on the ACS Publications website at DOI: 10.1021/acsami.9b10868.

Physical characterizations and electrochemical data analyses (PDF)

AUTHOR INFORMATION

Corresponding Authors

*E-mail: fchuang@mail.nsysu.edu.tw (F.-C.H.).

*E-mail: johnnyho@cityu.edu.hk (J.C.H.).

ORCID

Renjie Wei: 0000-0002-0459-7196

Xiuming Bu: 0000-0002-2372-2271

Wei Gao: 0000-0001-7606-7402

Changyong Lan: 0000-0002-5654-1098

Feng-Chuan Chuang: 0000-0003-0351-4253

Yongquan Qu: 0000-0002-6202-1929

Johnny C. Ho: 0000-0003-3000-8794

Notes

The authors declare no competing financial interest.

ACKNOWLEDGMENTS

We thank for the assistance of TEM from Prof. Fu-rong Chen and Mr. Tak Fu Hung. J.C.H. acknowledges the General Research Fund (CityU 11211317) and the Theme-Based Research Scheme (T42-103/16-N) of the Research Grants Council of Hong Kong SAR, China, the National Natural Science Foundation of China (Grant 51672229), and the Science Technology and Innovation Committee of Shenzhen Municipality (Grant JCYJ20170818095520778). F.-C.C. acknowledges support from the National Center for Theoretical Sciences and the Ministry of Science and Technology of Taiwan under Grants Number MOST-107-2628-M-110-001-MY3. He is also grateful to the National Center for High-Performance Computing for computer time and facilities.

REFERENCES

- (1) You, B.; Sun, Y. Innovative Strategies for Electrocatalytic Water Splitting. *Acc. Chem. Res.* **2018**, *51*, 1571–1580.
- (2) Suen, N.-T.; Hung, S.-F.; Quan, Q.; Zhang, N.; Xu, Y.-J.; Chen, H. M. Electrocatalysis for the Oxygen Evolution Reaction: Recent Development and Future Perspectives. *Chem. Soc. Rev.* **2017**, *46*, 337–365.
- (3) Fang, M.; Dong, G.; Wei, R.; Ho, J. C. Hierarchical Nanostructures: Design for Sustainable Water Splitting. *Adv. Energy Mater.* **2017**, *7*, 1700559.
- (4) Hunter, B. M.; Gray, H. B.; Müller, A. M. Earth-Abundant Heterogeneous Water Oxidation Catalysts. *Chem. Rev.* **2016**, *116*, 14120–14136.
- (5) Mondschein, J. S.; Callejas, J. F.; Read, C. G.; Chen, J. Y. C.; Holder, C. F.; Badding, C. K.; Schaak, R. E. Crystalline Cobalt Oxide Films for Sustained Electrocatalytic Oxygen Evolution under Strongly Acidic Conditions. *Chem. Mater.* **2017**, *29*, 950–957.
- (6) Chen, J. Y. C.; Miller, J. T.; Gerken, J. B.; Stahl, S. S. Inverse Spinel NiFeAlO_4 as a Highly Active Oxygen Evolution Electrocatalyst:

Promotion of Activity by a Redox-Inert Metal Ion. *Energy Environ. Sci.* **2014**, *7*, 1382.

(7) Kim, T. W.; Woo, M. A.; Regis, M.; Choi, K.-S. Electrochemical Synthesis of Spinel Type ZnCo_2O_4 Electrodes for Use as Oxygen Evolution Reaction Catalysts. *J. Phys. Chem. Lett.* **2014**, *5*, 2370–2374.

(8) Sickafus, K. E.; Wills, J. M.; Grimes, N. W. Structure of Spinel. *J. Am. Ceram. Soc.* **1999**, *82*, 3279–3292.

(9) Verwey, E. J. W.; de Boer, J. H. Cation Arrangement in a Few Oxides with Crystal Structures of the Spinel Type. *Recl. Trav. Chim. Pays-Bas* **1936**, *55*, 531–540.

(10) Dionigi, F.; Strasser, P. NiFe-Based (Oxy)Hydroxide Catalysts for Oxygen Evolution Reaction in Non-Acidic Electrolytes. *Adv. Energy Mater.* **2016**, *6*, 1600621.

(11) Liu, Y.; Xiao, C.; Huang, P.; Cheng, M.; Xie, Y. Regulating the Charge and Spin Ordering of Two-Dimensional Ultrathin Solids for Electrocatalytic Water Splitting. *Chem* **2018**, *4*, 1263–1283.

(12) Ooka, H.; Takashima, T.; Yamaguchi, A.; Hayashi, T.; Nakamura, R. Element Strategy of Oxygen Evolution Electrocatalysis Based on in Situ Spectroelectrochemistry. *Chem. Commun.* **2017**, *53*, 7149–7161.

(13) Wang, H.-Y.; Hung, S.-F.; Chen, H.-Y.; Chan, T.-S.; Chen, H. M.; Liu, B. In Operando Identification of Geometrical-Site-Dependent Water Oxidation Activity of Spinel Co_3O_4 . *J. Am. Chem. Soc.* **2016**, *138*, 36–39.

(14) Xu, L.; Jiang, Q.; Xiao, Z.; Li, X.; Huo, J.; Wang, S.; Dai, L. Plasma-Engraved Co_3O_4 Nanosheets with Oxygen Vacancies and High Surface Area for the Oxygen Evolution Reaction. *Angew. Chem. Int. Ed.* **2016**, *55*, 5277–5281.

(15) Wang, Y.; Zhou, T.; Jiang, K.; Da, P.; Peng, Z.; Tang, J.; Kong, B.; Cai, W.-B.; Yang, Z.; Zheng, G. Reduced Mesoporous Co_3O_4 Nanowires as Efficient Water Oxidation Electrocatalysts and Supercapacitor Electrodes. *Adv. Energy Mater.* **2014**, *4*, 1400696.

(16) Wei, R.; Fang, M.; Dong, G.; Lan, C.; Shu, L.; Zhang, H.; Bu, X.; Ho, J. C. High-Index Faceted Porous Co_3O_4 Nanosheets with Oxygen Vacancies for Highly Efficient Water Oxidation. *ACS Appl. Mater. Interfaces* **2018**, *10*, 7079–7086.

(17) Zhang, K.; Zhang, G.; Qu, J.; Liu, H. Disorder the Atomic Structure of Co(II) Oxide via B-Doping: An Efficient Oxygen Vacancy Introduction Approach for High Oxygen Evolution Reaction Electrocatalysts. *Small* **2018**, *14*, 1802760.

(18) Wang, H.-Y.; Hsu, Y.-Y.; Chen, R.; Chan, T.-S.; Chen, H. M.; Liu, B. Ni^{3+} -Induced Formation of Active NiOOH on the Spinel Ni-Co Oxide Surface for Efficient Oxygen Evolution Reaction. *Adv. Energy Mater.* **2015**, *5*, 1500091.

(19) Anindita; Singh, A.; Singh, R. N. Effect of V Substitution at B-Site on the Physicochemical and Electrocatalytic Properties of Spinel-Type NiFe_2O_4 towards O_2 Evolution in Alkaline Solutions. *Int. J. Hydrogen Energy* **2010**, *35*, 3243–3248.

(20) Jiang, J.; Sun, F.; Zhou, S.; Hu, W.; Zhang, H.; Dong, J.; Jiang, Z.; Zhao, J.; Li, J.; Yan, W.; Wang, M. Atomic-Level Insight into Super-Efficient Electrocatalytic Oxygen Evolution on Iron and Vanadium Co-Doped Nickel (Oxy)Hydroxide. *Nat. Commun.* **2018**, *9*, 2885.

(21) Liu, J.; Ji, Y.; Nai, J.; Niu, X.; Luo, Y.; Guo, L.; Yang, S. Ultrathin Amorphous Cobalt–Vanadium Hydr(Oxy)Oxide Catalysts for the Oxygen Evolution Reaction. *Energy Environ. Sci.* **2018**, *11*, 1736–1741.

(22) Sivakumar, P.; Ramesh, R.; Ramanand, A.; Ponnusamy, S.; Muthamizhchelvan, C. Preparation and Properties of Nickel Ferrite (NiFe_2O_4) Nanoparticles via Sol-Gel Auto-Combustion Method. *Mater. Res. Bull.* **2011**, *46*, 2204–2207.

(23) Trasatti, S.; Petrii, O. A. Real Surface Area Measurements in Electrochemistry. *J. Electroanal. Chem.* **1992**, *327*, 353–376.

(24) McCrory, C. C. L.; Jung, S.; Peters, J. C.; Jaramillo, T. F. Benchmarking Heterogeneous Electrocatalysts for the Oxygen Evolution Reaction. *J. Am. Chem. Soc.* **2013**, *135*, 16977–16987.

(25) Voiry, D.; Chhowalla, M.; Gogotsi, Y.; Kotov, N. A.; Li, Y.; Penner, R. M.; Schaak, R. E.; Weiss, P. S. Best Practices for Reporting

Electrocatalytic Performance of Nanomaterials. *ACS Nano* **2018**, *12*, 9635–9638.

(26) Hohenberg, P.; Kohn, W. Inhomogeneous Electron Gas. *Phys. Rev.* **1964**, *136*, B864–B871.

(27) Kohn, W.; Sham, L. J. Self-Consistent Equations Including Exchange and Correlation Effects. *Phys. Rev.* **1965**, *140*, A1133–A1138.

(28) Kresse, G.; Hafner, J. Ab Initio Molecular Dynamics for Liquid Metals. *Phys. Rev. B* **1993**, *47*, 558–561.

(29) Kresse, G.; Furthmüller, J. Efficient Iterative Schemes for Ab Initio Total-Energy Calculations Using a Plane-Wave Basis Set. *Phys. Rev. B* **1996**, *54*, 11169–11186.

(30) Perdew, J. P.; Burke, K.; Ernzerhof, M. Generalized Gradient Approximation Made Simple. *Phys. Rev. Lett.* **1996**, *77*, 3865–3868.

(31) Kresse, G.; Joubert, D. From Ultrasoft Pseudopotentials to the Projector Augmented-Wave Method. *Phys. Rev. B* **1999**, *59*, 1758–1775.

(32) Monkhorst, H. J.; Pack, J. D. Special Points for Brillouin-Zone Integrations. *Phys. Rev. B* **1976**, *13*, 5188–5192.

(33) Li, Q.; Wang, X.; Tang, K.; Wang, M.; Wang, C.; Yan, C. Electronic Modulation of Electrocatalytically Active Center of Cu_7S_4 Nanodisks by Cobalt-Doping for Highly Efficient Oxygen Evolution Reaction. *ACS Nano* **2017**, *11*, 12230–12239.

(34) Nørskov, J. K.; Rossmeisl, J.; Logadottir, A.; Lindqvist, L.; Kitchin, J. R.; Bligaard, T.; Jónsson, H. Origin of the Overpotential for Oxygen Reduction at a Fuel-Cell Cathode. *J. Phys. Chem. B* **2004**, *108*, 17886–17892.

(35) Yan, D.; Li, Y.; Huo, J.; Chen, R.; Dai, L.; Wang, S. Defect Chemistry of Nonprecious-Metal Electrocatalysts for Oxygen Reactions. *Adv. Mater.* **2017**, *29*, 1606459.

(36) Liu, Y.; Hua, X.; Xiao, C.; Zhou, T.; Huang, P.; Guo, Z.; Pan, B.; Xie, Y. Heterogeneous Spin States in Ultrathin Nanosheets Induce Subtle Lattice Distortion To Trigger Efficient Hydrogen Evolution. *J. Am. Chem. Soc.* **2016**, *138*, 5087–5092.

(37) Ling, T.; Yan, D.-Y.; Jiao, Y.; Wang, H.; Zheng, Y.; Zheng, X.; Mao, J.; Du, X.-W.; Hu, Z.; Jaroniec, M.; Qiao, S.-Z. Engineering Surface Atomic Structure of Single-Crystal Cobalt (II) Oxide Nanorods for Superior Electrocatalysis. *Nat. Commun.* **2016**, *7*, 12876.

(38) Zhang, R.; Zhang, Y.-C.; Pan, L.; Shen, G.-Q.; Mahmood, N.; Ma, Y.-H.; Shi, Y.; Jia, W.; Wang, L.; Zhang, X.; Xu, W.; Zou, J.-J. Engineering Cobalt Defects in Cobalt Oxide for Highly Efficient Electrocatalytic Oxygen Evolution. *ACS Catal.* **2018**, *8*, 3803–3811.

(39) Sun, Y.; Liu, Q.; Gao, S.; Cheng, H.; Lei, F.; Sun, Z.; Jiang, Y.; Su, H.; Wei, S.; Xie, Y. Pits Confined in Ultrathin Cerium(IV) Oxide for Studying Catalytic Centers in Carbon Monoxide Oxidation. *Nat. Commun.* **2013**, *4*, 2899.

(40) Biesinger, M. C.; Lau, L. W. M.; Gerson, A. R.; Smart, R. S. C. Resolving Surface Chemical States in XPS Analysis of First Row Transition Metals, Oxides and Hydroxides: Sc, Ti, V, Cu and Zn. *Appl. Surf. Sci.* **2010**, *257*, 887–898.

(41) Biesinger, M. C.; Payne, B. P.; Grosvenor, A. P.; Lau, L. W. M.; Gerson, A. R.; Smart, R. S. C. Resolving Surface Chemical States in XPS Analysis of First Row Transition Metals, Oxides and Hydroxides: Cr, Mn, Fe, Co and Ni. *Appl. Surf. Sci.* **2011**, *257*, 2717–2730.

(42) Hofmann, S. Qualitative Analysis (Principle and Spectral Interpretation). In *Auger- and X-Ray Photoelectron Spectroscopy in Materials Science: A User-Oriented Guide*; Springer, Berlin, Heidelberg, 2013; pp 43–76.

(43) Li, K.; Xue, D. Estimation of Electronegativity Values of Elements in Different Valence States. *J. Phys. Chem. A* **2006**, *110*, 11332–11337.

(44) Palmas, S.; Ferrara, F.; Vacca, A.; Mascia, M.; Polcaro, A. M. Behavior of Cobalt Oxide Electrodes during Oxidative Processes in Alkaline Medium. *Electrochim. Acta* **2007**, *53*, 400–406.

(45) Trotochaud, L.; Young, S. L.; Ranney, J. K.; Boettcher, S. W. Nickel–Iron Oxyhydroxide Oxygen-Evolution Electrocatalysts: The Role of Intentional and Incidental Iron Incorporation. *J. Am. Chem. Soc.* **2014**, *136*, 6744–6753.

(46) Yeo, B. S.; Bell, A. T. Enhanced Activity of Gold-Supported Cobalt Oxide for the Electrochemical Evolution of Oxygen. *J. Am. Chem. Soc.* **2011**, *133*, 5587–5593.

(47) Man, I. C.; Su, H.-Y.; Calle-Vallejo, F.; Hansen, H. A.; Martínez, J. I.; Inoglu, N. G.; Kitchin, J.; Jaramillo, T. F.; Nørskov, J. K.; Rossmeisl, J. Universality in Oxygen Evolution Electrocatalysis on Oxide Surfaces. *ChemCatChem* **2011**, *3*, 1159–1165.

(48) García-Mota, M.; Bajdich, M.; Viswanathan, V.; Vojvodic, A.; Bell, A. T.; Nørskov, J. K. Importance of Correlation in Determining Electrocatalytic Oxygen Evolution Activity on Cobalt Oxides. *J. Phys. Chem. C* **2012**, *116*, 21077–21082.

(49) Tao, H. B.; Xu, Y.; Huang, X.; Chen, J.; Pei, L.; Zhang, J.; Chen, J. G.; Liu, B. A General Method to Probe Oxygen Evolution Intermediates at Operating Conditions. *Joule* **2019**, 1498–1509.

(50) Indra, A.; Menezes, P. W.; Sahraie, N. R.; Bergmann, A.; Das, C.; Tallarida, M.; Schmeißer, D.; Strasser, P.; Driess, M. Unification of Catalytic Water Oxidation and Oxygen Reduction Reactions: Amorphous Beat Crystalline Cobalt Iron Oxides. *J. Am. Chem. Soc.* **2014**, *136*, 17530–17536.

(51) Yang, Y.; Fei, H.; Ruan, G.; Xiang, C.; Tour, J. M. Efficient Electrocatalytic Oxygen Evolution on Amorphous Nickel–Cobalt Binary Oxide Nanoporous Layers. *ACS Nano* **2014**, *8*, 9518–9523.

(52) Kwon, G.; Jang, H.; Lee, J.-S.; Mane, A.; Mandia, D. J.; Soltau, S. R.; Utschig, L. M.; Martinson, A. B. F.; Tiede, D. M.; Kim, H.; Kim, J. Resolution of Electronic and Structural Factors Underlying Oxygen-Evolving Performance in Amorphous Cobalt Oxide Catalysts. *J. Am. Chem. Soc.* **2018**, *140*, 10710–10720.